A&A 418, 163–176 (2004)
DOI: 10.1051/0004-6361:20034176
© ESO 2004

Astronomy & Astrophysics

An excitation study of bow shocks driven from protostars in S233IR⋆

T. Khanzadyan[1], M. D. Smith[2], C. J. Davis[3], and T. Stanke[4]

[1] MPI für Astronomie, Königstuhl 17, 69117 Heidelberg, Germany
[2] Armagh Observatory, Armagh BT61 9DG, Northern Ireland, UK
e-mail: mds@star.arm.ac.uk
[3] Joint Astronomy Centre 660 N. A'Ohoku Place, University Park, Hilo, Hawaii 96720, USA
e-mail: c.davis@jach.hawaii.edu
[4] MPI für Radioastronomie, Auf dem Hügel 69, 53121, Bonn, Germany
e-mail: tstanke@mpifr-bonn.mpg.de

Received 11 August 2003 / Accepted 19 January 2004

Abstract. We present narrow-band near-infrared images of the high-mass star formation region S233IR. We detect several groups of molecular hydrogen knots aligned with known outflows. Images in vibrationally-excited H_2 and [Fe II] reveal the excitation distributions across the main two conspicuous bow shocks. Emission from the [Fe II] line is strong and located at the apex of both bow shocks as well as other locations within the northern bow where we distinguish a compact Mach disk through its [Fe II] emission. The H_2 emission is not restricted to the bow wings but distinct components are detected near the bow apices. The data are broadly comparable to steady bow shocks of speed 60–80 km s^{-1} possessing dissociative caps and C-type flanks. Nevertheless, non-steady bow shock behavior is essential to interpret all aspects of the bow structures. In this respect, the S233 bow caps may be in the neutral transformation stage from J-type to C-type.

Key words. infrared: ISM – stars: formation – ISM: jets and outflows – ISM: clouds

1. Introduction

Some of the gas attempting to accrete onto protostars is driven into collimated outflows which disturb and disrupt their environments (Bally & Lada 1983; Bachiller 1996; Richer et al. 2000; Reipurth & Bally 2001). The outflows sweep up, compress and excite cloud material in their paths through shock waves. As part of our program to scrutinise these environments, we here present high resolution near-infrared images of the outflows in the S233 HII region. This region contains high mass protostars within dense molecular cores (Porras et al. 2000). We aim to constrain the properties of the outflows, determine the significance of the feedback from the protostar and estimate the physical conditions in the ambient molecular cloud.

S233 contains two young star clusters, located near the IRAS source 05358+3543, which has a luminosity of 6300 $L_\odot$ (Hodapp 1994; Porras et al. 2000; Jiang et al. 2001). The youngest cluster is centered on S233IR and associated with IRAS 05358+3543 mm (Beuther et al. 2002a). High mass protostars are still forming in this region as evidenced by maser emission (see Tofani et al. 1995; Wouterloot et al. 1988; Menten 1991) and strong outflow activity (Beuther et al. 2002a). At least three outflows emanate from the central region.

The most extended outflow appears to terminate in two prominent H_2 bow shocks, N1 and N6 (Porras et al. 2000; Kumar et al. 2002). The peak H_2 emission from the N1 bow is blueshifted (−25.2 km s^{-1}) while that from N6 is redshifted (−17.3 km s^{-1}) but consistent with the cloud radial speed (−17.6 km s^{-1}) (Beuther et al. 2002a). Although these radial velocity shifts are low, it cannot be concluded that the outflow is near to the plane of the sky since H_2 lines tend to peak near the ambient cloud speed whatever the orientation (Smith & Brand 1990; Davis et al. 2000). A highly collimated bipolar CO outflow, outflow A, is closely aligned with the N1−N6 H_2 outflow. The radial speeds, however, appear contrary, with redshifted CO 1–0 emission mainly along the flow axis towards N1 in the north and blueshifted emission along the axis towards the south (Beuther et al. 2002a). The radial speeds are typically only a few km s^{-1} and so suggest a flow near the plane of the sky. This flow is also interesting for its asymmetry: not only is the outflow bent towards the east (i.e. a C-symmetry), but the southern Bow N6 lies roughly 1.4 times further away from IRAS 05358+3543 mm than N1. We shall refer to IRAS 05358+3543 mm as the driving protostar.

Send offprint requests to: T. Khanzadyan,
e-mail: khtig@mpia-hd.mpg.de

⋆ Based on observations collected at the UK Infrared Telescope, which is operated by the Joint Astronomy Centre on behalf of the UK Particle Physics and Astronomy Research Council.

Article published by EDP Sciences and available at http://www.aanda.org or http://dx.doi.org/10.1051/0004-6361:20034176

A second cluster of young stellar objects lies ∼40″ to the south-west, corresponding to 0.5 pc at the assumed distance to S233 of 1.8 kpc. This cluster is estimated to be older although young stars are still deeply embedded (Porras et al. 2000) and H_2 is seen in a narrow ring encircling a NIR star, attributed to fluorescence (Kumar et al. 2002).

Besides disordered clumps and knots, S233 contains examples of bright bow shocks. The narrow-band images presented here are of excited molecular and atomic gas, in the H_2 2−1 S(1) line at 2.247 μm and the [Fe II] line at 1.64 μm. These are supplemented by a new H_2 1−0 S(1) image to permit us to test models for the bow shocks through detailed geometric and physical modelling. We may thus (1) determine the necessary driving power, (2) address the debate concerning the shock physics (e.g. C-type or J-type), (3) test the assertion that a Mach Disk is present in the N1 bow (Kumar et al. 2002), (4) limit the speeds of the bows and (5) distinguish separate shock fronts through the spatial distribution of excitation.

Only a few bow shocks have been previously imaged in H_2 lines originating from above the first vibrational level (Davis & Smith 1995; Eislöffel et al. 1996). Recent studies of HH7 and HH240 have both concluded that C-type shock physics with paraboloidal bow shocks are responsible (Smith et al. 2003; O'Connell et al. 2004). Here, after presenting (Sect. 2) and discussing (Sect. 3) the new data, we adapt the models developed for those studies in order to model these bow shocks (Sect. 4).

The S233 region is located in the Perseus Arm. A distance of 1.8 kpc has been adopted due to its location near IRAS 05358+3543, as in earlier investigations by Evans & Blair (1981); Wilking et al. (1989); Snell et al. (1990); Henning et al. (1992). Molecular line observations reveal that the entire region within S231, S233 and S235 has a gas column density $N_{H_2} = 6 \times 10^{21}$ cm^{-2} and mass $M_{H_2} = 450\ M_\odot$ (Casoli et al. 1986). In contrast, the submillimeter core contains 600 $M_\odot$ with a mean column of $N_{H_2} = 6 \times 10^{23}$ cm^{-2} and mean density 9.3×10^5 cm^{-3}. Three sub-cores contain ∼100 $M_\odot$ each with a mean column of $N_{H_2} = 5 \times 10^{24}$ cm^{-2} (Beuther et al. 2002a). It is thus clear that the large-scale near-infrared structure should be strongly influenced by extinction.

2. Observations and data analysis

2.1. UFTI observations

Observations of the S233IR region were carried out on the night of December 10, 2000 with the Fast Track Imager (UFTI) installed at the 3.8 m United Kingdom Infrared Telescope (UKIRT), on the summit of Mauna Kea, Hawaii. The UFTI camera has a 1024 × 1024 pixel HgCdTe array and with internal optics providing a pixel scale of 0.091 arcsec. This provides a total field of view of 1.55 × 1.55 arcmin^2.

Images were obtained in the v = 1–0 S(1) transition of H_2 using a 1 percent narrow-band filter centered at $\lambda = 2.122\ \mu$m with $FWHM = 0.02\ \mu$m as well as in the [Fe II] line filter centered at $\lambda = 1.644\ \mu$m with $FWHM = 0.016\ \mu$m. For continuum subtraction purposes images in a K[98] broad band filter centered at $\lambda = 2.2\ \mu$m were also obtained during that night. Data reduction proceeded through standard routines which are presented in Khanzadyan et al. (2003); Chrysostomou et al. (2000).

2.2. IRCAM3 observations

The S233IR-N1 and N6 bows were also observed on December 11, 2000 using a newly reconfigured IRCAM3 camera installed on UKIRT. The IRCAM3 has a 256 × 256 InSb array with a scale of 0.081 arcsec per pixel which provides a total field of view 20.8 × 20.8 arcsec^2. Images were obtained in the v = 2−1 S(1) transition of H_2 using a narrow-band filter centered at $\lambda = 2.25\ \mu$m with $FWHM = 0.04\ \mu$m. Data reduction again proceeded through the above cited methods (Khanzadyan et al. 2003; Smith et al. 2003).

2.3. Omega prime observations

We have used an H band (centered at $\lambda = 1.646\ \mu$m) image obtained on December 23, 1999 using Omega Prime (Bizenberger et al. 1998) at the Calar Alto 3.5 m telescope. Omega Prime is equipped with a Rockwell 1024 × 1024 pixel HAWAII array detector with a scale of 0.4 arcsec per pixel which provides a total field of view of 6.8 × 6.8 arcmin^2. Data reduction was performed by the standard methods described in McCaughrean et al. (2004).

2.4. Continuum subtraction

2.4.1. H_2 1–0 S(1) line

To identify the pure H_2 1–0 S(1) line emission we subtracted the images obtained in the K[98] broad band filter using the following approach. First the images have been aligned, then PSFs (Point Spread Functions) for stars on both images were constructed. Next, a comparison of PSFs from both images enabled us to determine a scaling factor, Const. between the fluxes of both profiles. Then we used Const. to scale down the K[98] filter image which was then used to subtract the continuum from the H_2 1–0 S(1) line image.

This approach gives satisfactory results when identifying pure H_2 1–0 S(1) shocked material but, due to color differences in the field stars, this can still leave some residuals with point sources. To correct this we performed further "tuning" of Const. in order to subtract all stars present in the field. The last operation didn't change significantly Const. from the original value (∼15%).

2.4.2. [Fe II] line

To identify pure [Fe II] line emission features on the UFTI image we have rebinned it to match the Omega Prime H band image pixel scale, then the procedure used for H_2 1–0 S(1) line continuum subtraction was also applied here to identify the pure [Fe II] line emission objects. In this way we have identified pure [Fe II] emission only from the N1, N2A and N6 knots (see further).

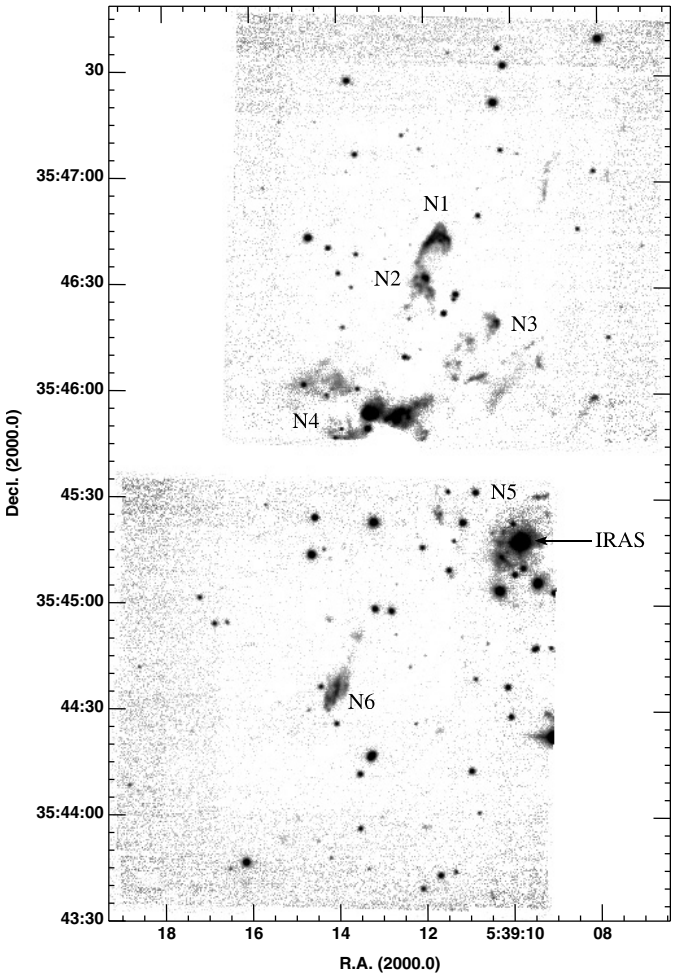

Fig. 1. The S233IR region in H_2 1-0 S(1) line + Continuum. Knots found by Porras et al. (2000) are marked N1 to N6 and the position of the IRAS source 05358+3543 is also indicated.

2.5. Creating ratioed images

To compare our results with the bow shock models we have created ratioed images of 2–1/1–0 S(1) H_2 using the following approach: from the beginning we were obliged to match the *FWHM* seeing for all images used in our analysis due to different pixel scales and variable seeing during observations of H_2 1−0 S(1) and [Fe II] line images (0.7–0.9 arcsecs). Therefore the IRCAM 2–1 S(1) H_2 image was binned up to 0.162 arcsec/pix scale in order to increase S/N ratio. Then UFTI images (H_2 1–0 S(1) and [Fe II] lines) binned up to 0.162 arcsec/pix scale again increasing S/N ratio and matching the pixel scale. The resulting images were checked for *FWHM* seeing and smoothed with 2D Gaussian in order to match the *FWHM* seeing (0.9 arcsecs on the final images). In the last step the images were aligned, scaled and divided.

3. Results

3.1. The S233IR region

S233IR in H_2 1–0 S(1) is displayed in Fig. 1. The image consists of two non-overlapping fields (North and South). The images have been astrometrically calibrated and then mosaicked to represent the entire area. The previously known N1–N6 knots as well as the IRAS source 05358+3543 are marked on the image. The integration time of the entire area presented in Fig. 1 in H_2 1–0 S(1) is 1620s.

Figure 1 reveals considerably more features and fine-scale structure than in Porras et al. (2000), (900 s on 2.1 m telescope). A superb UKIRT/UFTI H_2 1–0 S(1) image revealed detailed fine structure in the northern lobe with only 600 s exposure (Kumar et al. 2002).

Figure 2 shows pure H_2 1–0 S(1) emission line images of S233IR North(a) and South(b) regions. Continuum is subtracted using the approach described above. However, one can see that, due to the presence of reflection in the central region of S233IR, there are some remnants of imperfect continuum subtraction. Our results agree with McCaughrean et al. (2004) who overcome this by using a continuum line filter which has the same width and is free from contamination of other H_2 lines in the *K* broad band.

Table 1 lists the details of all knots which have been identified on continuum subtracted H_2 1–0 S(1) line observations. The naming of individual knots is the same as McCaughrean et al. (2004). The first three columns identify the knots. The fourth to sixth columns list detected flux values in H_2 1–0 S(1), H_2 2–1 S(1) and [Fe II] emission in units of 10^{-19} W m^{-2} for the indicated circular apertures. The background noise level for all three narrow-band observations is measured within a 6″ circular aperture in more than 10 object-free positions and averaged to yield error given in Table 1. Remarks on individual knots are given in the seventh column and explained at the bottom of Table 1.

3.2. Individual objects

3.2.1. N1A, N1B, and N6A

Only the bright bows N1, the compact knot N2A, and the counter-jet bow shock N6A were observed in all three filters.

The N1 bow complex is shown in Fig. 3. The panels display [Fe II], H_2 1–0 S(1) and H_2 2–1 S(1) images. The flux levels, indicated by color bars, are in units of 10^{-19} W m^{-2} arcsec^{-2}. Offsets are measured from the peak value on the H_2 1–0 S(1) image. Prior to this, the images were aligned pair by pair, e.g. [Fe II] line and H_2 1–0 S(1) images were wide enough to contain more than 10 identical field stars. Then, to align the 2−1 S(1) H_2 image with the 1–0 S(1), we have aligned the N2 bow peak. In this way the error of alignment in both cases was on order of one pixel (∼0.1 arcsecs).

The N6A bow structure is also presented in the three narrow-band filters in Fig. 4. Offsets are measured from the IR Star, which was used to align the images with high accuracy. As in the case of N1, colour-bars represent flux level in 10^{-19} W m^{-2} arcsec^{-2}.

3.2.2. N2 knots

N2A is present in the lower part of Fig. 3. Coverage of the entire knot was not performed. This particular knot has a very strong, star-like peak but its shock-excited nature is

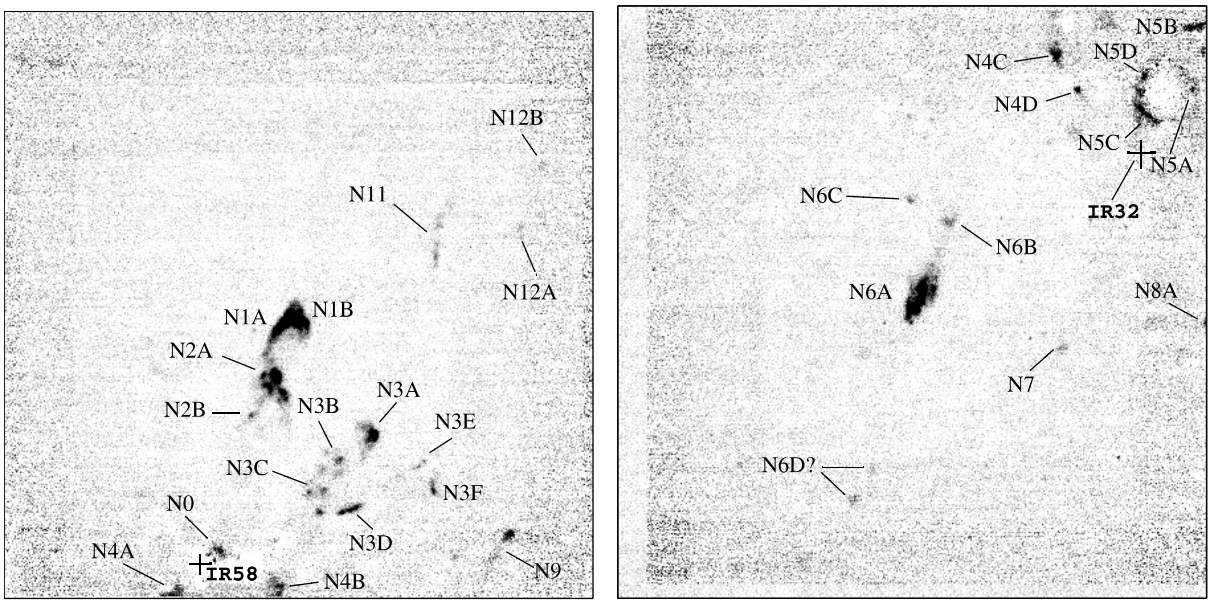

(a) North (b) South

Fig. 2. H_2 1–0 S(1) continuum subtracted images of the S233IR region (see Sect. 2.4). Identified knots are marked as in Porras et al. (2000) and McCaughrean et al. (2004) and listed in Table 1. Panel **a)** displays the northern part, where the "+" sign marks the location of the IR58 infrared source from Porras et al. (2000) ($05^h39^m13^s.3$; +35°45′53″.8) for a reference. Panel **b)** shows the southern part, where the "+" sign marks the location of IR32 infrared source ($05^h39^m09^s.6$; +35°45′05″.9) for a reference. The image sizes are roughly 2.1′ × 2.1′.

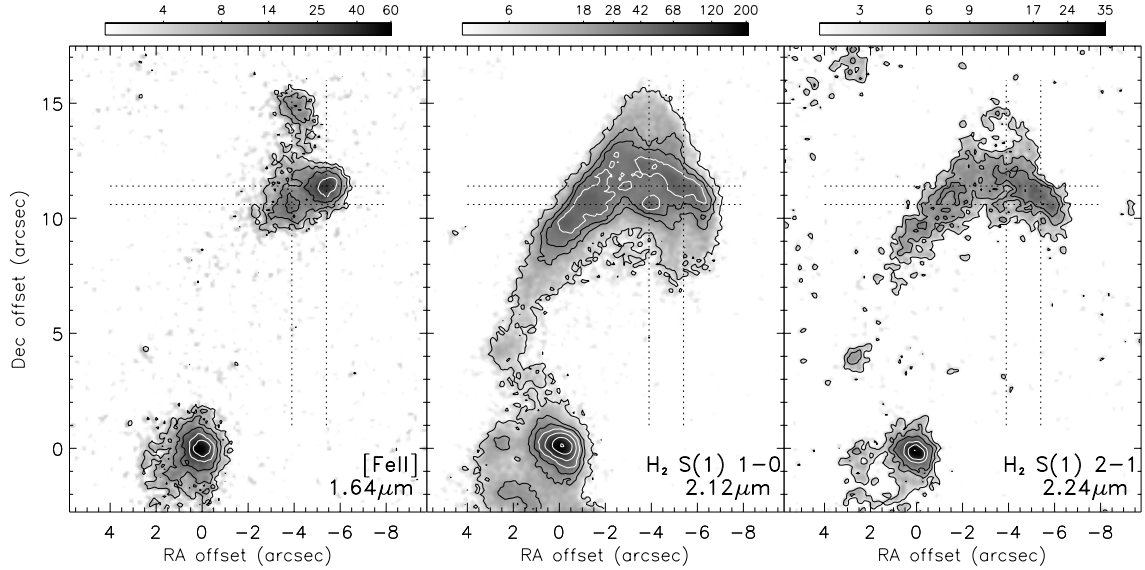

Fig. 3. The N1A+N1B bow and part of the N2A bow in three excitation lines (as indicated on each image). Offsets are measured from the N2A bow peak (see Table 1). North is up and east is left. Dot-dashed lines show the positions of [Fe II] peak and the Mach Disk proposed by Kumar et al. (2002) on each image. Continuum is not subtracted. Color bars represent flux levels in 10^{-19} W m^{-2} arcsec^{-2} and give values for contour levels. The integration times for [Fe II], 1–0 S(1) and 2–1 S(1) were 1620 s, 1620 s and 3600 s respectively.

demonstrated by the low 2–1/1–0 ratio. A more detailed view of N2A is presented in Fig. 5 (upper part), where one can see its complex structure, consisting of several shock fronts.

3.2.3. N3 complex and N0 knot

This complex consists of six individual knots A to F (see Fig. 1). One can separate the knots according to potential flow directions from the center of the cluster, as was also attempted by Kumar et al. (2002). In particular, knots N3A and N3B can be aligned with knot N0 and possibly with N4A on the far side of the core (see Figs. 1 and 5). However, the "gap" between the two sections undermines the possibility of a clear counter-flow detection on the opposite side of the core region. The N3C knot could well have some connection with this flow.

The remaining knots in this group may also represent one separate flow which is almost parallel to the flow described above. Figure 5 shows that N3D, N3E and possibly N3F are

Table 1. Knots detected in H_2 S(1) 1–0 line observations.

Knot Name	RA (2000.0)	Dec (2000.0)	S(1) 1–0 †,♣ (2.122 μm)	S(1) 2–1 †,♣ (2.248 μm)	[Fe II] †,♣ (1.644 μm)	Remarks
N0	$05^h39^m13\overset{s}{.}0$	+35°45′56″	430.2 (2.″7)	no obs.	no det.	b
N1	$05^h39^m11\overset{s}{.}9$	+35°46′42″	1276 (17″)	212.0 (19″)	-	a
N1A	$05^h39^m11\overset{s}{.}9$	+35°46′42″	680.8 (7″)	96.6 (7″)	no det.	a
N1B	$05^h39^m11\overset{s}{.}5$	+35°46′43″	502.1 (7″)	98.9 (7″)	125.7 (7″)	a
N2A	$05^h39^m11\overset{s}{.}9$	+35°46′32″	765.7 (9.″6)	94.3 (6″)	136.6 (6″)	a
N2B	$05^h39^m12\overset{s}{.}4$	+35°46′24″	26.3 (4.″6)	no obs.	no det.	b
N3A	$05^h39^m10\overset{s}{.}4$	+35°46′19″	273.9 (8″)	no obs.	no det.	a
N3B	$05^h39^m10\overset{s}{.}9$	+35°46′14″	97.8 (9.″3)	no obs.	no det.	a
N3C	$05^h39^m11\overset{s}{.}5$	+35°46′08″	95.1 (9.″3)	no obs.	no det.	a
N3D	$05^h39^m10\overset{s}{.}8$	+35°46′04″	126.8 (6″)	no obs.	no det.	a
N3E	$05^h39^m09\overset{s}{.}6$	+35°46′13″	5.6 (6.″2)	no obs.	no det.	b
N3F	$05^h39^m09\overset{s}{.}4$	+35°46′08″	66.9 (5.″8)	no obs.	no det.	b
N4A	$05^h39^m14\overset{s}{.}1$	+35°45′46″	202.5 (5.″8)	no obs.	no det.	a, c
N4B	$05^h39^m12\overset{s}{.}1$	+35°45′46″	128.7 (5.″8)	no obs.	no det.	a, c
N4C	$05^h39^m11\overset{s}{.}7$	+35°45′25″	115.8 (5.″8)	no obs.	no det.	a
N4D	$05^h39^m11\overset{s}{.}4$	+35°45′18″	29.6 (2.″7)	no obs.	no det.	b
N5A	$05^h39^m09\overset{s}{.}4$	+35°45′17″	222.4 (4.″2)	no obs.	no det.	a
N5B	$05^h39^m09\overset{s}{.}4$	+35°45′30″	60.8 (6″)	no obs.	no det.	a
N5C	$05^h39^m10\overset{s}{.}0$	+35°45′15″	587.6 (6″)	no obs.	no det.	b
N5D	$05^h39^m10\overset{s}{.}3$	+35°45′17″	382.1 (6″)	no obs.	no det.	b
N6A	$05^h39^m14\overset{s}{.}1$	+35°44′35″	838.5 (2 × 7″)	70.9 (2 × 7″)	162.8 (2 × 7″)	a
N6B	$05^h39^m13\overset{s}{.}6$	+35°44′50″	43.6 (6.″3)	no det.	no det.	b
N6C	$05^h39^m14\overset{s}{.}2$	+35°44′55″	11.4 (4″)	no det.	no det.	b
N6D	$05^h39^m15\overset{s}{.}3$	+35°43′53″	35.2 (4″)	no obs.	no det.	b
N7C	$05^h39^m07\overset{s}{.}4$	+35°47′14″	18.9 (5″)	no obs.	no det.	b
N7	$05^h39^m09\overset{s}{.}2$	+35°44′20″	17.1 (4.″2)	no obs.	no det.	b
N9	$05^h39^m08\overset{s}{.}1$	+35°45′58″	96.1 (4.″3)	no obs.	no det.	b
N11	$05^h39^m09\overset{s}{.}3$	+35°46′57″	31.1 (7″)	no obs.	no det.	b
N12A	$05^h39^m07\overset{s}{.}9$	+35°47′01″	18.9 (5″)	no obs.	no det.	b
N12B	$05^h39^m07\overset{s}{.}5$	+35°47′14″	15.1 (5″)	no obs.	no det.	b

† Flux in 10^{-19} W m^{-2} units calculated over indicated circular aperture.
♣ Background 1σ noise estimate in 6″ circular aperture for H_2 S(1) 1–0 is 3.7×10^{-19} W m^{-2}, 5.9×10^{-19} W m^{-2} for H_2 S(1) 2–1, and 2.9×10^{-19} W m^{-2} for [Fe II] observations.
Remarks: (a) Knot is reported by Porras et al. (2000). (b) Definition of knot by McCaughrean et al. (c) There is no full coverage of this knot.

connected with an elongated fuzzy reflection feature which is connected to the core region. One can also relate a part of the N3C knot to this distinctive flow. The existence of a second flow can explain the position of the N3C knots.

Knot N0 is situated near the core of the S233IR region and is associated with bright reflection (see Fig. 5). The nearest embedded source IR58 (Porras et al. 2000) could be the driving source, but one should obtain enough observational facts to state this explicitly.

3.2.4. N4 knots

Porras et al. (2000) associated components A, B and C to knot N4. Here, we add knot D which is clearly visible in Fig. 2b. Due to the fact that N4A and N4B are situated on the edge of the observed region in the north of S233IR, the flux values given in Table 1 are unreliable.

3.2.5. N5 knots

This group of objects are distributed mainly around the cluster of stars which harbours IRAS 05358+3543. Here we also complement the list of Porras et al. (2000) by adding three new knots (N5C, D and E).

Here we would like to note that Kumar et al. (2002) using UFTI images reported an additional knot in N5 group, which was also identified on our UFTI images. However, by comparing our results with the images from McCaughrean et al. (2004) we realised that the new found knot is a ghost caused by the bright star (e.g., Fig. 1).

3.2.6. N7 and N8 knots

These knots are identified only after continuum subtraction (see Sect. 2.4). From our pictures, however, it is still not clear to which outflow structure the N7 knot belongs but, its position

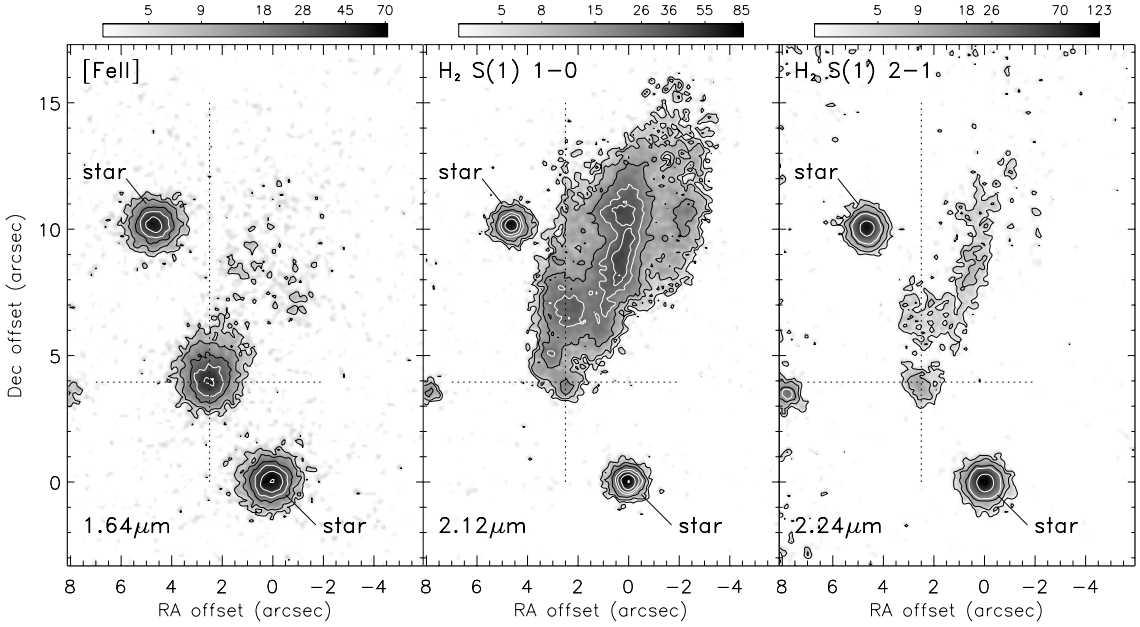

Fig. 4. The N6 bow in three different excitation lines as presented for N1 in Fig. 3. Offsets are measured from the IR7 infrared source (Porras et al. 2000) ($05^h39^m14^s.1$; $+35°44'26''.2$). The dot-dashed line shows the [Fe II] peak position on all images.

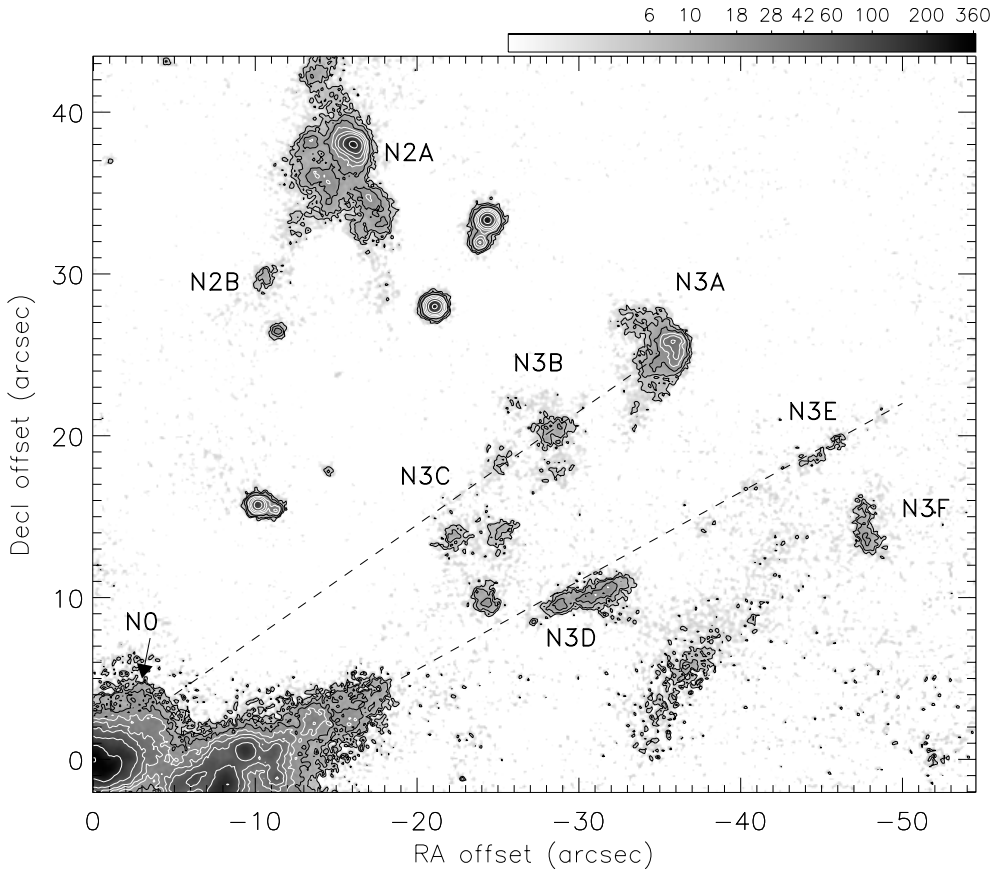

Fig. 5. The N3 complex in H_2 1–0 S(1) + continuum. Offsets are measured from the bright IR58 infrared source ($05^h39^m13^s.3$; $+35°45'53''.8$). North is up and east is left. The color bar represents the flux level in units of 10^{-19} W m^{-2} arcsec^{-2} and give values for contour levels. Dashed lines indicate possible outflow directions (see text).

suggests a connection with Outflow C, recognised by Beuther et al. (2002a) in CO and SiO emission.

The N8 knot is almost out of our field and is not presented in Table 1 but it is associated with the bright star just on the edge of our southern field (see Fig. 1).

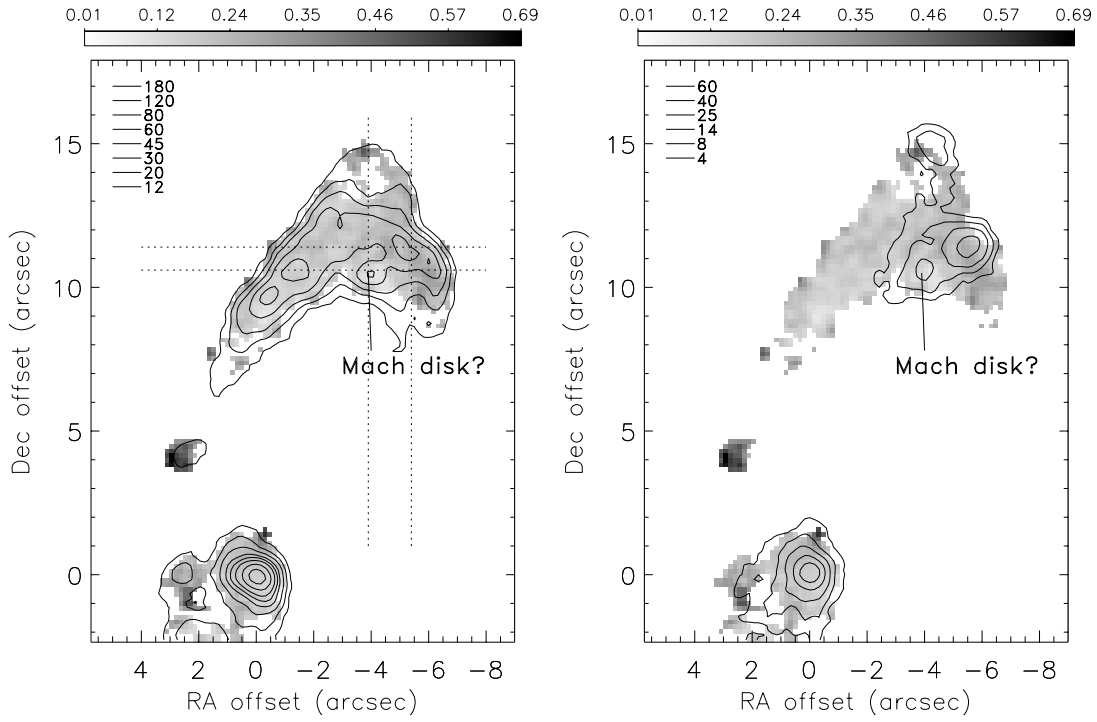

(a) N1 & N2A + H_2 1–0 S(1) contours (b) N1 & N2A + [Fe II] contours

Fig. 6. H_2 2–1/1–0 S(1) ratio images of the N1 bow and part of the N2A bow overlaid with H_2 1–0 S(1) **a)** and [Fe II] **b)** contours. Contour levels are given on each panel. Dot-dashed lines on the left panel indicate the position of the high [Fe II] emission peak and the Mach Disk proposed by Kumar et al. (2002).

3.2.7. N9, N11, N12A and N12B

We mark the N9 outflow structure just in the south-west corner of Fig. 2a. It has an elongated tail-like appearance which indicates that this flow may come from the older cluster associated with the IRAS 05358+3543 source.

N11 is a filamentary structure which is again identified only after continuum subtraction (see Fig. 2a). Its elongation indicates that this is a jet-like structure but the origin of the flow is unknown.

N12A and N12B are knots which are part of a faint group situated to the north west of S233IR; these are also presented by McCaughrean et al. (2004). This group of knots are also associated with Outflow C, seen in CO and SiO emission (Beuther et al. 2002a).

3.3. N1–N6 outflow

N1, N2, and N6 together represent an outflow which originates from the IR cluster of stars (see Fig. 1). The outflow extent from tip to tip is 2′:21″ (141″) which converts to a projected length of 1.24 pc (cluster distance = 1.8 kpc). The dynamical age of the outflow is 6×10^3 years if the bows move with a proper motion of 100 km s^{-1}.

Additionally we have identified two more H_2 knots (N6D) further south (see Fig. 2) from N6A. These may be the remnants of yet another bow shock in the N1–N6 outflow, created in an outburst preceding the one responsible for creating the N1/N6 bows.

3.4. 2–1/1–0 S(1) H_2 Images

In this section we describe 2–1/1–0 S(1) H_2 ratio images created according to the approach described in Sect. 2.5. Figure 6 represents ratio image of the N1 bow and part of the N2A bow overlaid with H_2 1–0 S(1) line (panel a) and with [Fe II] line (panel b), offsets are measured from the N2A knot. Figure 7 shows the same for the N6 bow where offsets are measured from the IR star at the lower part of the figure. Color bars on both pictures represent the 2–1/1–0 ratio.

4. General interpretation

4.1. Parameters

We present here general constraints on the N1–N6 outflow as preparation for the specific modelling. There are four aspects to the constraints: size, power, structure and excitation.

The separations and projected distances of the bows from the driving protostar are 56″(1.51×10^{18} cm) and 85″(2.29×10^{18} cm) for N1 and N6, respectively, for the assumed distance of 1.8 kpc. The transverse scale of the leading H_2 bow shocks is about 5″, which we equate to $2R_{\rm bow} = 1.3 \times 10^{17}$ cm.

The H_2 1–0 S(1) luminosities are 0.013 $L_\odot$ (N1), 0.009 $L_\odot$ (N6) and 0.029 $L_\odot$ (total, N1, N2 and N6 knots). This implies a total H_2 luminosity in all rotational and vibrational lines of ∼0.3–0.6 $L_\odot$, corresponding to a wide range in excitations through either C-type or J-type shocks (Smith 1995). The total outflow power necessary to drive these shocks lies between 3–30 $L_\odot$ before any extinction correction, according to either

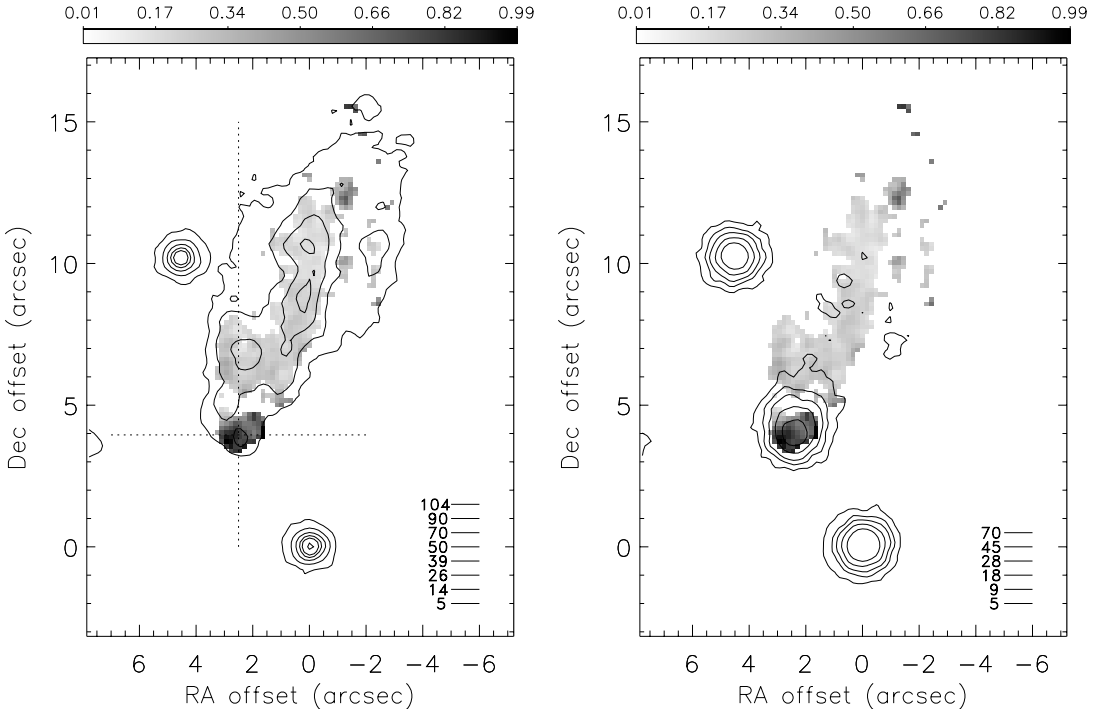

(a) N6 + H_2 1–0 S(1) contours (b) N6 + [Fe II] contours

Fig. 7. H_2 2–1/1–0 S(1) ratio images of the N6 bow overlaid with H_2 1–0 S(1) **a)** and [Fe II] **b)** contours. Contour levels are given on each panel. The dot-dashed line on the left panel indicate the position of high [Fe II] emission peak.

bow shock models or hydrodynamic simulations (Smith 1991; Rosen & Smith 2003, 2004b).

The theoretical rate (P) at which a bow of speed $v_{\rm bow}$ converts the driving power into heat is written in the form

$$P = 43\left(\frac{n}{1\times10^4\ {\rm cm^{-3}}}\right) \times\left(\frac{v_{\rm bow}}{100\ {\rm km\ s^{-1}}}\right)^3\left(\frac{R_{\rm bow}}{6.7\times10^{16}\ {\rm cm}}\right)^2 L_\odot, \quad (1)$$

to an order of magnitude, where n is the density of hydrogen nucleons (and the mass density is $\rho = 2.32\times10^{-24}\,n$, including 10% helium atoms).

As an estimate of the density in the environments of the bow shocks we will take $n = 10^4\,{\rm cm^{-3}}$. This is consistent with the average density of $\sim3\times10^4\,{\rm cm^{-3}}$ within half the outflow scale of 0.8×10^{18} cm, derived from the reported optical extinction of ∼15 mag to young stars located within a radius of 30″ of the driving source (Porras et al. 2000). Our choice also finds support in the modelling of the wings of CO rotational lines, Beuther et al. (2002a) conclude that densities of $10^4\,{\rm cm^{-3}}$ would be sufficient to thermalize the CO to the observed level. A significantly higher density is implausible since then the near-infrared extinction correction would indicate an intrinsic outflow power in excess of the bolometric luminosity.

On adjusting for extinction with this density, the intrinsic outflow power is estimated to be 20–100 $L_\odot$ from the observed near-infrared data. This is a reasonable fraction of the bolometric luminosity and is also comparable to the mechanical luminosity of the CO outflow of 9.1 $L_\odot$ (Beuther et al. 2002b).

Note that a low density of $10^3\,{\rm cm^{-3}}$ would imply no extinction correction in the near-infrared and an outflow power ∼3–30 $L_\odot$. This is also consistent with the observed mechanical luminosity. However, for the theoretical power P to also be consistent then requires the bow speed to be above 85 km s^{-1}. As will be shown, the images suggest lower bow speeds.

The excitation image of the N1 bow (Fig. 6) shows interesting structure. The 2–1/1–0 ratio is 0.1–0.2 over most of the bow area. This is consistent with collisional excitation (Black & Dalgarno 1976; Shull & Beckwith 1982). However, a patch of somewhat higher (∼0.3–0.4) 2–1/1–0 ratio is located in the bright, western wing of the N1 bow, where also most of the [Fe II] emission is generated (Figs. 3 and 6b). This could be the location of the Mach disk, where the driving supersonic jet is presently being braked (Kumar et al. 2002). On the other hand, the second brightest knot in the [Fe II] line (marked as "Mach disk?" in Fig. 6) coincides with the Mach disk proposed by Kumar et al. (2002). Although it corresponds to a H_2 1–0 S(1) knot, it does not coincide with a high 2–1/1–0 ratio. This would suggest that the point of jet impact has recently moved to the west.

There is also weak H_2 emission from the bow cap with [Fe II] emission from the tip and trail. Note that the southern counterpart, bow N6, also possesses weak high excitation emission from the apex (Figs. 4 and 7b). This suggests that dissociative J-shocks are responsible for the excitation (e.g. Smith 1994b) at the leading edges.

The N6 bow has a more compact structure. We note the strong [Fe II] line emission generated from the apex of the bow, possibly caused by a direct impact of the jet at the leading

edge whereas the impact in N1 is on the oblique shock wing. Emission from H_2, however, is not completely absent at the apex. More puzzling is the strong H_2 2–1 S(1) emission from this region also. As shown in Fig. 6b, the 2–1/1–0 line ratio reaches 0.6, which is consistent with excitation of molecules by UV fluorescence (Black & Dalgarno 1976; Shull & Beckwith 1982).

At first sight, for both bows (N1 and N2A) one can drive parallels with the HAMMER-jet models described by Suttner et al. (1997a) and Völker et al. (1999). In these three dimensional hydrodynamic simulations of molecular jets into molecular clouds, multiple curved structures both with curved arcs (run 3D-1) and more compact conical structures (3D-2) were uncovered.

The N6 bow can also be interpreted as a superposition of bows. The following bow preserves most of its H_2 and even populates the second excitation level. But the leading bow moves faster and destroys the H_2. This is consistent with a HAMMER-type jet model which produces multiple bows with different speeds. The detailed modelling below will indicate whether two curved shocks are necessary.

5. The bow model

Are the arc-shaped structures really bow shocks? To help answer this, we have attempted to model the bows as steady MHD flows in which the shock front has a fixed geometry. The original models for C-shocks (CBOW, Smith & Brand 1990)) and J-shocks (JBOW, Smith 1994a) have been recently refined and applied to resolved bow shocks in HH7 (Smith et al. 2003) and HH240 (O'Connell et al. 2004). We apply this latest version here.

There are many basic constraints for N1 and N6 which limit the modelling from the outset. The motion is close to the plane of the sky, the density is near $10^4\,\mathrm{cm}^{-3}$ and the transverse extents are 2.2×10^{17} cm (N1) and 1.6×10^{17} cm (N2). We take position angles of 347.2° (N1) and 167.2° (N6) for the directions of motion of the bows in the plane of the sky.

Emission at 1.64 μm from [Fe II] has now been found in a number of bow shocks (e.g. Nisini et al. 2002). To generate [Fe II] emission, we require the presence of fast dissociative shocks. Therefore, the emission must arise from a different part of the shock surface than producing the molecular emission. The [Fe II] emission is expected from the bow cap and molecular emission from the bow flanks, as displayed by the prototypical example HH99 (Davis et al. 1999). This clearly also holds in the N1 and N6 bows. For this reason, the ratio of iron to molecular hydrogen emission, [Fe II]/1–0 S(1), over entire bow shocks can take a wide range of values within the range 0.1–10.

Fast shocks are efficient in destroying dust grains, releasing heavy elements back into the interstellar medium. These elements are usually strongly depleted under normal conditions. Iron is a typical example of such an element with a free abundance in the local interstellar medium of $\sim1.4\times10^{-6}$, 5% of that tied up in grains. The bow codes calculate only basic chemical processes and essential molecular transitions. This is because the shock surface is split up into many hundreds of thousands of distinct planar shock elements, making a simplified shock treatment computationally necessary. In some circumstances, the number of independent shock integrations are reduced to a few hundred by symmetry arguments (i.e. if the magnetic field and bow shock direction coincide and the bow is in the plane of the sky). To facilitate the calculation, we adopt an expression for the [Fe II] emission given by Smith (1994b), assuming non-LTE conditions and modified by a free iron abundance of 0.05 ϵ(Fe) for $v < 60\,\mathrm{km\,s^{-1}}$ and

$$\varepsilon(\mathrm{Fe}) = 0.05 + 0.95\left(\frac{v - 60\ \mathrm{km\ s^{-1}}}{v}\right)^2 \epsilon(\mathrm{Fe_o}) \qquad (2)$$

for $v > 60\,\mathrm{km\,s^{-1}}$, $\epsilon(\mathrm{Fe_o}) = 3\times10^{-5}$, based on the results presented by Jones et al. (1996) for shock sputtering of grains. Here, ϵ(Fe)n is the total available iron density and v is the shock speed (transverse to the bow surface). Furthermore, we run trials with two analytical expression for the electron fraction in order to gauge the sensitivity to this factor. We took $n_e = 0.1$, a constant, and $n_e = \eta/(\eta+1)$ where $\eta = (v/80\,\mathrm{km\,s^{-1}})^{3.3}$ and v is the shock speed and found no significant difference.

5.1. J-type bow shock for N1

A simulated J-type bow shock is displayed in Fig. 8. Most important is the low bow speed of $50\,\mathrm{km\,s^{-1}}$ necessary to generate strong molecular emission in the flanks near the bow cap rather than in the far tail. Comparing the H_2 structure with N1 (Fig. 3), the predicted molecular wings are narrower but more extended than observed. The [Fe II] knot at the apex is reproduced but the knot within the bow wing is not predicted and requires another origin.

We have simulated the 2–1/1–0 ratio image in Fig. 9. It is evident that the excitation distribution also matches that observed quite well (Fig. 6), in that no gradient is predicted over most of the bow. The predicted excitation level of the brightest section ~0.2–0.3 is marginally higher than observed (~0.15–0.25) as is the ratio of the totals (see Table 2). In addition, the overall luminosity is predicted given 2.5 mag of K-band extinction (see Table 2).

One issue left unexplained in the J-shock model is the existence of weak 1–0 S(1) emission from the bow cap. Furthermore, how can the molecular section be J-type when the bow is so deeply embedded? If the ion fraction is low, we expect ambipolar diffusion to control the physics and the shock to be C-type. Finally the high peak [Fe II] and total emission predicted from the bow cap could be problematic although, as shown in Table 2, the intrinsic [Fe II] emission may be several times larger than observed when extinction is taken into account.

On the other hand, the structure of the northern lobe of the CO bipolar outflow is also left unexplained. The CO outflow is displaced laterally from the H_2 flow (Beuther et al. 2002b). This could partly be a result of the low bow speed, allowing CO (and Fe) to remain depleted. This is, however, difficult to reconcile with the implied release of CO closer to the driving source.

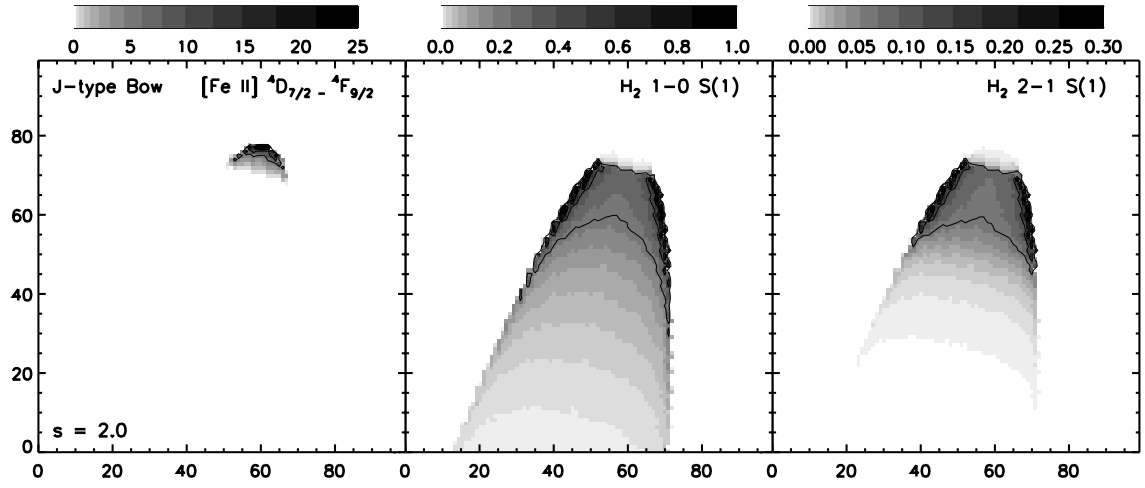

Fig. 8. A J-type bow shock model for bow N1: a paraboloidal bow moving in the plane of the sky. Parameters are: $v_{\rm bow} = 50\,{\rm km\,s^{-1}}$, $n = 10^4\,{\rm cm^{-3}}$, 10 pixels = $R_{\rm bow} = 6.7 \times 10^{16}$ cm, magnetic field = 54 μG (Alfvén speed = 1 km s^{-1}) directed along the bow path, oxygen abundance of 4×10^{-4} and carbon abundance of 2×10^{-4}.

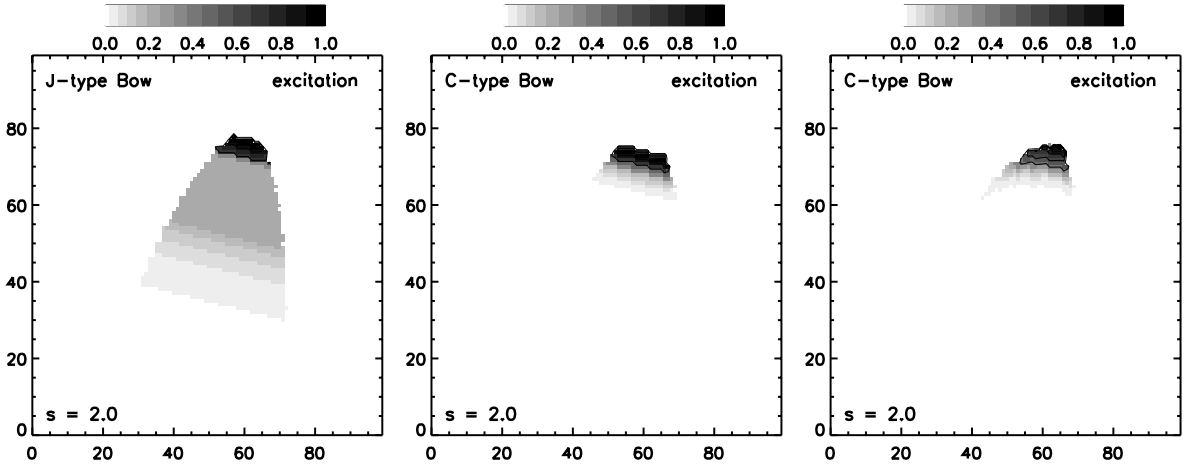

Fig. 9. Vibrational excitation of molecular hydrogen within J-type (*left*), C-type with parallel field (*middle*) and C-type bow with an oblique field (*right panel*). The images are displayed in Figs. 8 and 10. These are simulated images of the H_2 vibrational excitation represented by the ratio of line fluxes from the 2–1 S(1) and 1–0 S(1) lines.

Table 2. Luminosities in solar units and luminosity ratios.

Bow	L(1–0 S(1)) $\times 10^{-4}\,L_\odot$	L(2–1)/L(1–0) ratio	L([Fe II])/L(1–0) ratio
N1 ($A_K = 0$)	128	0.166	0.099
N1 ($A_K = 2.5$)	1260	0.134	0.346
J-Bow (50 km s^{-1})	1480	0.186	1.40
C-Bow (65 km s^{-1})	2250	0.144	1.66
C-Bow (65 km s^{-1}) (asymm. mag. field)	2290	0.158	1.45
N6 ($A_K = 0$)	93	0.076	0.175
N6 ($A_K = 2.5$)	920	0.061	0.612
J-Bow (76 km s^{-1})	1290	0.186	1.40
C-Bow (76 km s^{-1}, s = 1.5)	9560	0.106	0.348
C-Bow (76 km s^{-1}, s = 1.5, asymm. field)	9580	0.092	0.346

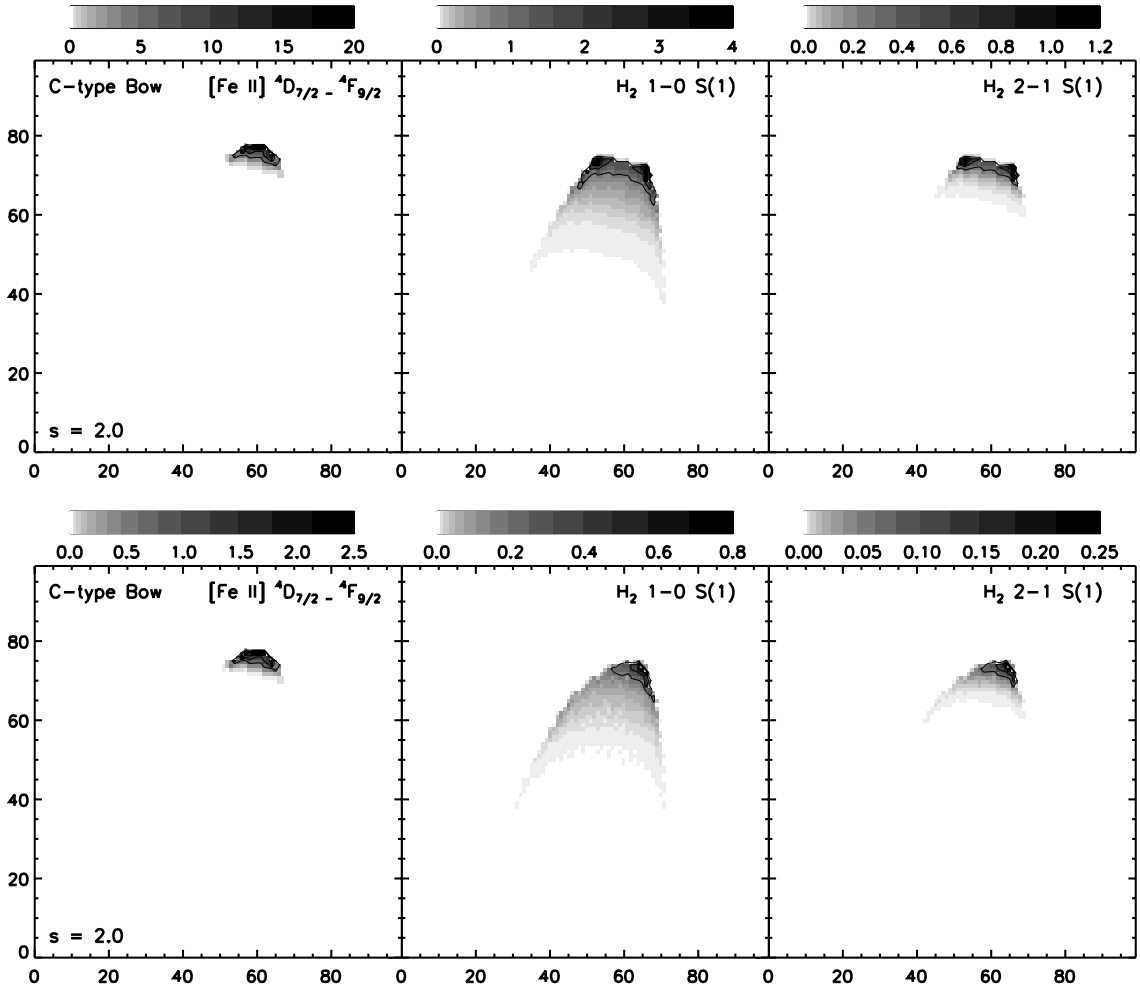

Fig. 10. C-type bow shock models for bow N1: a paraboloidal bow moving in the plane of the sky. Parameters are: $v_{\rm bow}$ = 65 km s^{-1}, n = 10^4 cm^{-3}, ion fraction = 3×10^{-6}, 10 pixels = $R_{\rm bow}$ = 6.7×10^{16} cm, magnetic field = 54 μG (Alfvén speed = 1 km s^{-1}), oxygen abundance of 4×10^{-4} and carbon abundance of 2×10^{-4}. In the upper panel, the magnetic field is directed along the bow path; in the lower panel, an oblique magnetic field at 45° to the bow axis is taken.

5.2. C-type bow shock for N1

A bow shock of speed 65 km s^{-1} provides the best C-type shock fit to the H_2 emission structure, as shown in Fig. 10. Higher speeds tend to push the emission into two separated wings. The [Fe II] emission from the C-type section is negligible. Strong iron emission arises from the fast dissociative shock around the bow cap.

The simulated C-type bow slightly overproduces in all the lines although the excitation is similar to that observed. It is not straightforward to reduce the luminosities except by reducing the density. This, however, would most likely reduce the extinction and so reduce the intrinsic flux. More serious, however, is the distribution of vibrational excitation shown in the middle panel of Fig. 9, which shows a steep gradient in excitation, unlike the smooth observed distribution.

The magnetic field is critical to C-shock structure. The above model assumed a parallel field which tends to soften and cool the wings providing a steep excitation gradient. We have therefore also modelled the bow with a field at 45° to the bow direction of motion but still in the plane of the sky. The lower panel of Fig. 10 shows an asymmetric structure with tails extending to 10″ (1 pixel = 0.5″). The excitation diagram also shows a somewhat more extended structure (Fig. 9).

We are led to a scenario in which the present bow shock has been formed by a jet entering, sweeping and distorting a thick clump of molecular gas. In this case, the H_2 emission can be strong, being the snapshot of the present impact region while the CO emission, which records the history of the flow, reveals other locations where dense gas is spread more uniformly. In this respect, we propose that the bow N1 represents the abrupt entry of the shock into a clump. In principle, the wings are either J-type (until a magnetic precursor has time to develop) or C-type. The bow cap, however, is already half way into the transition from a dissociative J-shock into a C-type shock and so emits weak H_2 emission from a strengthening magnetic precursor. The time taken for an ion precursor to develop is quite short (a few years), proceeding at the ion-magnetosonic speed (Smith & Mac Low 1997). The development of the neutral deceleration zone occurs during the "neutral transformation" stage which proceeds at the Alfvén speed, $v_{\rm A}$, as has been shown through numerical simulations

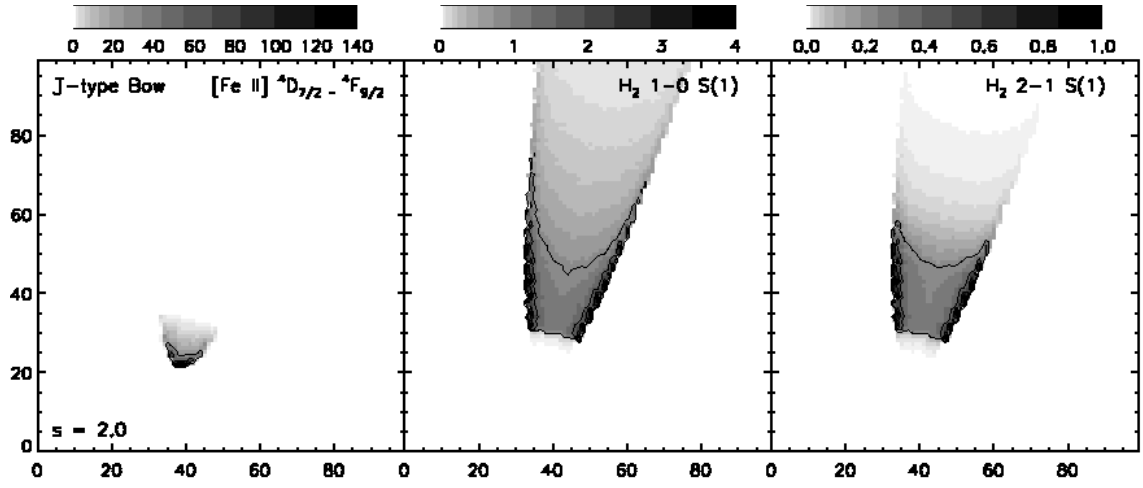

Fig. 11. A J-type bow shock model for bow N6: a paraboloidal bow moving in the plane of the sky. Parameters are: $v_{\rm bow} = 76\,{\rm km\,s^{-1}}$, $n = 10^4\,{\rm cm^{-3}}$, 10 pixels = $R_{\rm bow} = 3.3\times10^{16}$ cm, magnetic field = 54 μG (Alfvén speed = 1 km s^{-1}) directed along the bow path, oxygen abundance of 4×10^{-4} and carbon abundance of 2×10^{-4}.

(Smith & Mac Low 1997; Chieze et al. 1998). The eventual neutral C-shock length length is

$$L_{\rm c} \sim 8\times10^{15}\,\frac{v_{\rm A}}{n_i\,v_{\rm shock}}\ {\rm cm}, \qquad (3)$$

(Smith & Brand 1990) where n_i is the ion density (with a value of 0.03 cm^{-3} in the C-type shocks calculated above). Therefore, for a C-shock of width 4×10^{15} cm to develop takes $L_{\rm c}/v_{\rm A} \sim 1300$ yr with $v_{\rm A} = 1\,{\rm km\,s^{-1}}$. This compares well to the dynamical time 2 $R_{\rm bow}/v_{\rm bow} \sim 1000$ yr of the flow through the bow but is considerably shorter than the dynamical time of the outflow of ∼6000 yr. We conclude that the bow N1 is most likely progressing through a highly turbulent medium with structure on the scale of $R_{\rm bow}$ and is in a process of physical transformation.

There are several alternative means of producing H_2 emission from shocks. Firstly, the H_2 would be collisionally excited on entering a fast dissociative shock before complete dissociation takes place. Although some emission will originate from this zone, it is very narrow and the time available for spontaneous decay is extremely short in comparison with that from extended cooling layers behind shock waves. Secondly, the H_2 would reform after being destroyed in a fast dissociative shock. To collisionally excite this gas, however, would require another shock. Thirdly, the dense layer of reformed molecules could be fluorescently excited by extreme ultraviolet radiation. Given the low bow speeds, however, a source of UV radiation is not evident.

Fourthly, the H_2 cap emission could consist of dust-scattered H_2 photons which have their origin in the C-type bow flanks. The potential scattering layer is the compressed post-shock gas. The problem is to hold the gas within this layer against the deflection and expansion into the bow tail which tends to limit the scattering column to $\sim n\,R_{\rm bow} \sim 7\times10^{20}$ cm^{-2} for the fiducial values – sufficient to provide a few per cent scattering of incident near-infrared photons. This mechanism has been invoked to explain optical line emission in the vicinity of the HH 1 bow shock by Noriega-Crespo et al. (1991). For N1, this is a viable mechanism because the bow shock is so large. Fifthly, we may be observing two superimposed bow shocks, with a weaker and slower bow shock being, in projection, overtaken by an independently driven bow. Sixthly, the structure could develop as a result of hydrodynamic impacts from a non-steady jet-cloud interaction as uncovered in the numerical simulations of hammer jets (Völker et al. 1999). In this interpretation, N1 constitutes at least 2 bows. We detect [Fe II] and enhanced excitation at the leading edges, as predicted by the models. Similarly for N6, there is enhanced 2–1/1–0 and [Fe II] emission in the bow cap. The hammer jet model also accounts for features along the flow such as the N2 system in terms of shock structures.

5.3. J-type bow shock for N6

The bow N6 images are modelled by taking a bow speed of 76 km s^{-1}, the value predicted by the N6–N1 separation ratio and the N1 bow speed for a J-type shock. As shown in Fig. 11, the higher speed of N6 results in the H_2 emission being generated from a long tail with a strong [Fe II] knot occupying the apex. The shape is again a paraboloid but the scale $R_{\rm bow}$ is half that of N1, hence giving the appearance of higher collimation. The narrower bow may thus be powered by a slightly better focussed jet but with the same rate of flow of momentum as its northern counterpart. A major problem again with the J-shock model is the length of the tail, which is 25″(50 pixels) in 1−0 S(1) emission, in comparison to the observed 10″.

The exceedingly low overall excitation of N6 is especially difficult to reproduce with any J-type shock (see Table 2). A lower density would lower the collisional excitation into the second vibrational level but then problems arise with the power and extinction constraints.

5.4. C-type bow shock for N6

To produce the longer tail of 1–0 S(1) emission with a C-type shock, we simulate a bow with relatively stronger shocks in the wings by taking a more conical bow shape (Fig. 12). Again,

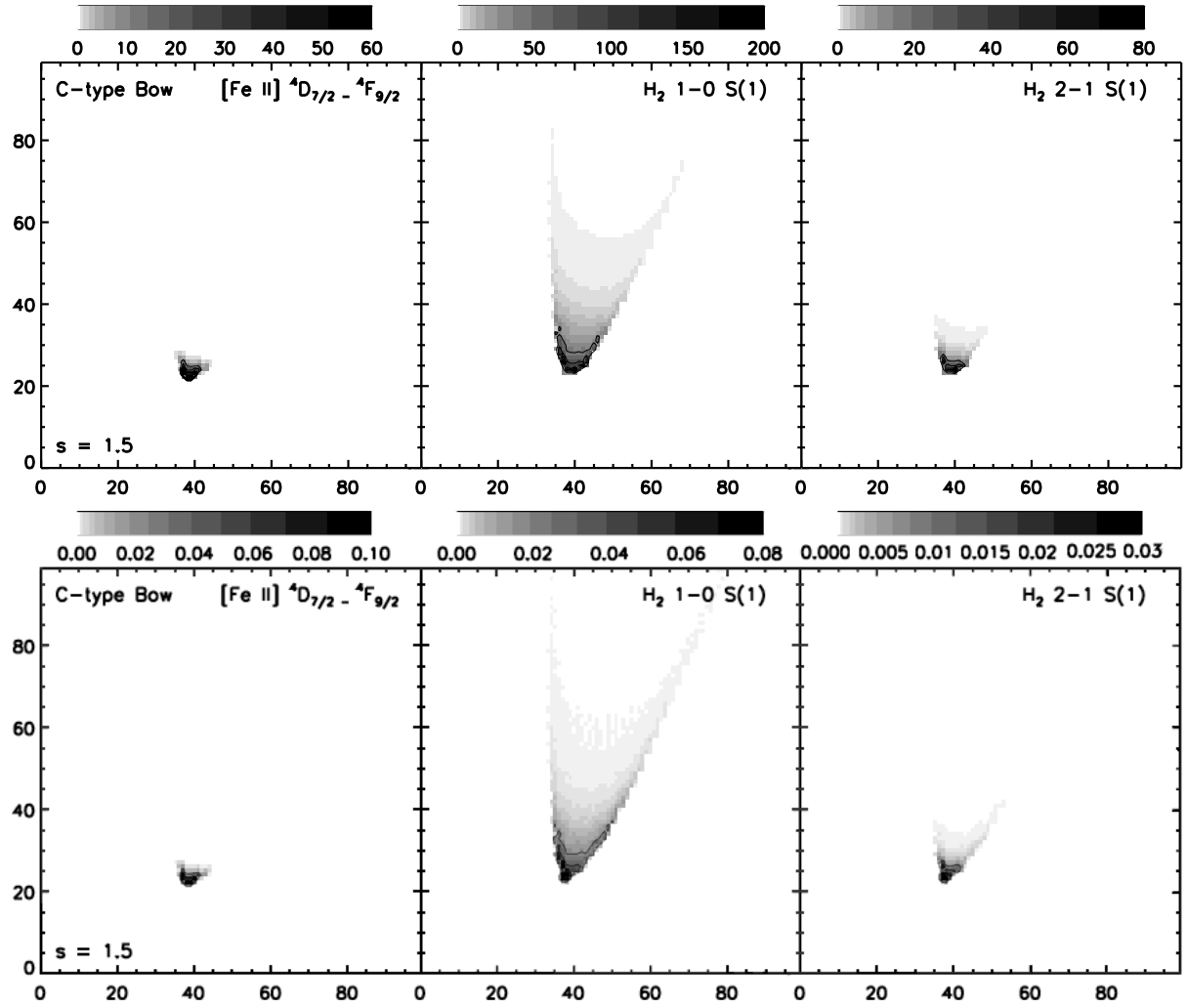

Fig. 12. C-type bow shock models for bow N6: a bow with shape $z \propto R^s$ with $s = 1.5$ in cylindrical coordinates, moving in the plane of the sky. Parameters are: $v_{\rm bow} = 76\,{\rm km\,s^{-1}}$, $n = 10^4\,{\rm cm^{-3}}$, 10 pixels = $R_{\rm bow} = 3.3 \times 10^{16}$ cm, magnetic field = $54\,\mu$G (Alfvén speed = $1\,{\rm km\,s^{-1}}$), oxygen abundance of 4×10^{-4} and carbon abundance of 2×10^{-4}. In the upper panel, the magnetic field is directed along the bow path; in the lower panel, an oblique magnetic field at 45° to the bow axis is taken.

a C-shock generates strong 1–0 S(1) emission and the excitation, although now considerably lower due to the more aerodynamic shape, is still high in comparison to the observed value. Given the considerable fine-scale structure, and possible striations across the bow, some weak turbulence may be dissipating in the bow wake, producing low-excitation emission.

An asymmetric magnetic field improves the fit (Fig. 12 lover panel). A compact knot appears at the apex location where the field inhibits dissociation and an enhanced flank is also produced. The tail length, however, appears somewhat shorter than observed.

6. Conclusions

We have recorded numerous H_2 features associated with several outflows in the S233 field. This extends the near infrared studies of Porras et al. (2000) and Kumar et al. (2002). We tentatively detect two H_2 knots (N6D) further south than previously found in the N1–N6 (outflow A). This may be their final resting place, where the outflow momentum is exhausted. We also detect groups of knots which are associated with the southern (N7) and northern (N12) lobes of Outflow C, recognised by (Beuther et al. 2002a) in CO and SiO emission.

Our main purpose was to measure the excitation within the strong H_2 bow-shaped shocks by also imaging in the H_2 2–1 S(1) and [Fe II] emission lines. We found that flux and excitation distributions correspond to bow shocks.

Bow speeds under $80\,{\rm km\,s^{-1}}$ are predicted. We have attempted to model the more distant southern bow N6 with a faster bow than the northern N1, with the idea that they were both produced in the same explosive event from the driving source. The faster speed of N6 then produces a more aerodynamic shape which can partly account for the lower molecular excitation. This counter-intuitive effect (since a faster *planar shock* would mean higher excitation) was uncovered in 3D numerical simulations of molecular flows (Rosen & Smith 2004a). The faster southern bow could be the result of a better focussed jet or a lower density ambient medium. A lower density medium would also contribute to the lower H_2 excitation through a reduction in collisional excitation.

J-type shock models tend to produce bows with quite high excitation and long wings. C-type bows can better reproduce the observed emission patterns and sizes especially with an oblique magnetic field. C-type shocks, however, generate stronger H_2 emission than observed and slightly shorter tails

Asymmetry in the H_2 bows and excitation image can be produced by an asymmetric magnetic field. There is, however, strong [Fe II] emission from within N1 which may well correspond to a Mach disk where a driving jet hits an oblique layer of swept-up material, as originally suggested by (Kumar et al. 2002) on the basis of a strong compact 1–0 S(1) peak.

Atomic emission is detected from the apex of both bows, as expected for dissociative shock caps. The suggested higher speed of bow N6 is consistent with its relatively stronger atomic emission. For N1, the paraboloidal model tends to produce more [Fe II] than observed, which suggest a lower iron abundance or electron fraction than assumed here. For N6, the conical bow shape restricts the area of the bow cap, producing a compact peak.

Finally, the N1 bow contains H_2 emission spread over the bow apex where we expect only atomic gas. Reforming molecules would be too cool to be vibrationally excited and fluorescent excitation is ruled out by the low bow speed. We suggested in Sect. 5.2 that, since molecular clouds are turbulent and clumpy, the bow is now entering a denser region and the shock is in the transition process of forming a magnetic precursor closer to the apex. The impact may be responsible for some of the fine-scale structure which is even more prominent on the 1–0 S(1) image of Kumar et al. (2002). The time required for molecular shocks to reach a steady state can be extremely long in star formation regions, possibly exceeding the flow dynamical time, as calculated for S233 in Sect. 5.2.

Three other plausible explanations are discussed in Sect. 5.2. These are: dust-scattering of H_2 photons from the bow flanks, projected independent bow shocks and time-variable bow shock dynamics.

Near-infrared spectroscopic data would now be useful to determine the extinction and, hence, to confirm the bow power. Spectroscopy will also determine the departure from local thermodynamic equilibrium and, hence, the cause of the low population in the second vibrational level of molecular hydrogen.

Acknowledgements. We would like to acknowledge the data analysis facilities provided by the Starlink Project which is run by CCLRC / Rutherford Appleton Laboratory on behalf of PPARC. In addition, the following Starlink packages have been used: CCDPACK, KAPPA and GAIA.

References

Bachiller, R. 1996, ARA&A, 34, 111
Bally, J., & Lada, C. J. 1983, ApJ, 265, 824
Beuther, H., Schilke, P., Gueth, F., et al. 2002a, A&A, 387, 931
Beuther, H., Schilke, P., Sridharan, T. K., et al. 2002b, A&A, 383, 892
Bizenberger, P., McCaughrean, M. J., Birk, C., Thompson, D., & Storz, C. 1998, in Proc. SPIE, 3354, 825, Infrared Astronomical Instrumentation, ed. A. M. Fowler, 825
Black, J. H., & Dalgarno, A. 1976, ApJ, 203, 132
Casoli, F., Combes, F., Dupraz, C., Gerin, M., & Boulanger, F. 1986, A&A, 169, 281
Chieze, J.-P., Pineau des Forets, G., & Flower, D. R. 1998, MNRAS, 295, 672
Chrysostomou, A., Hobson, J., Davis, C. J., Smith, M. D., & Berndsen, A. 2000, MNRAS, 314, 229
Davis, C. J., Berndsen, A., Smith, M. D., Chrysostomou, A., & Hobson, J. 2000, MNRAS, 314, 241
Davis, C. J., & Smith, M. D. 1995, ApJ, 443, L41
Davis, C. J., Smith, M. D., Eislöffel, J., & Davies, J. K. 1999, MNRAS, 308, 539
Eislöffel, J., Smith, M. D., Davis, C. J., & Ray, T. P. 1996, AJ, 112, 2086
Evans, N. J. & Blair, G. N. 1981, ApJ, 246, 394
Henning, T., Cesaroni, R., Walmsley, M., & Pfau, W. 1992, A&AS, 93, 525
Hodapp, K. 1994, ApJS, 94, 615
Jiang, Z., Yao, Y., Yang, J., et al. 2001, AJ, 122, 313
Jones, A. P., Tielens, A. G. G. M., & Hollenbach, D. J. 1996, ApJ, 469, 740
Khanzadyan, T., Smith, M. D., Davis, C. J., et al. 2003, MNRAS, 338, 57
Kumar, M. S. N., Bachiller, R., & Davis, C. J. 2002, ApJ, 576, 313
McCaughrean, M. J., Stanke, T., Andersen, M., Beuther, H., & Quirrenbach, A. 2004, A&A, in preparation
Menten, K. M. 1991, ApJ, 380, L75
Nisini, B., Caratti o Garatti, A., Giannini, T., & Lorenzetti, D. 2002, A&A, 393, 1035
Noriega-Crespo, A., Boehm, K., & Calvet, N. 1991, ApJ, 379, 676
O'Connell, B., Smith, M. D., Hodapp, K., Davis, C. J., & Khanzadyan, T. 2004, MNRAS, submitted
Porras, A., Cruz-González, I., & Salas, L. 2000, A&A, 361, 660
Reipurth, B., & Bally, J. 2001, ARA&A, 39, 403
Richer, J. S., Shepherd, D. S., Cabrit, S., Bachiller, R., & Churchwell, E. 2000, Protostars and Planets IV, 867
Rosen, A., & Smith, M. D. 2003, MNRAS, 343, 181
Rosen, A., & Smith, M. D. 2004a, MNRAS, in press
Rosen, A., & Smith, M. D. 2004b, A&A, 413, 593
Shull, J. M., & Beckwith, S. 1982, ARA&A, 20, 163
Smith, M. D. 1991, MNRAS, 253, 175
Smith, M. D. 1994a, MNRAS, 266, 238
Smith, M. D. 1994b, A&A, 289, 256
Smith, M. D. 1995, A&A, 296, 789
Smith, M. D., & Brand, P. W. J. L. 1990, MNRAS, 245, 108
Smith, M. D., Khanzadyan, T., & Davis, C. J. 2003, MNRAS, 339, 524
Smith, M. D., & Mac Low, M.-M. 1997, A&A, 326, 801
Snell, R. L., Dickman, R. L., & Huang, Y.-L. 1990, ApJ, 352, 139
Suttner, G., Smith, M. D., Yorke, H. W., & Zinnecker, H. 1997a, A&A, 318, 595
Tofani, G., Felli, M., Taylor, G. B., & Hunter, T. R. 1995, A&AS, 112, 299
Völker, R., Smith, M. D., Suttner, G., & Yorke, H. W. 1999, A&A, 343, 953
Wilking, B. A., Blackwell, J. H., Mundy, L. G., & Howe, J. E. 1989, ApJ, 345, 257
Wouterloot, J. G. A., Henkel, C., & Brand, J. 1988, A&A, 191, 323